

pubs.acs.org/ac Article

Enhanced Characterization of Histones Using 193 nm Ultraviolet Photodissociation and Proton Transfer Charge Reduction

Jada N. Walker, Raymond Lam, and Jennifer S. Brodbelt*



Cite This: Anal. Chem. 2023, 95, 5985-5993



Read Online

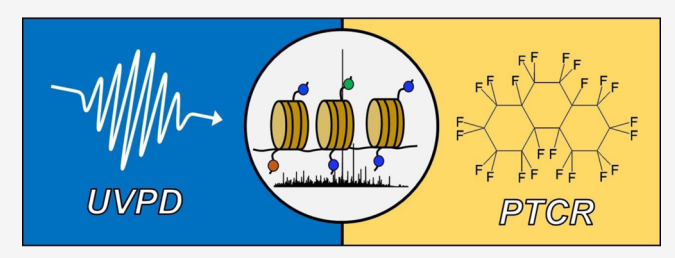
ACCESS I

Metrics & More

Article Recommendations

Supporting Information

ABSTRACT: Top-down characterization of histones, proteins that are critical participants in an array of DNA-dependent processes, offers the potential to examine the relationship between histone structure and mechanisms of genetic regulation. Mapping patterns of post-translational modifications (PTMs) of histones requires extensive backbone cleavages to bracket the sites of mass shifts corresponding to specific PTMs. Ultraviolet photodissociation (UVPD) causes substantial fragmentation of proteins, which is well-suited for PTM localization, but the resulting spectra are



congested with fragment ions that may have overlapping isotopic distributions that confound deconvolution. Gas-phase proton transfer charge reduction (PTCR) decreases the charge states of highly charged ions, thus alleviating this congestion and facilitating the identification of additional sequence-determining and PTM-localizing fragment ions. By integrating UVPD with PTCR for histone proteoform analyses, sequence coverages up to 91% were achieved for calf thymus histone H4 containing acetylation marks at the N-terminus and Lys12 as well as a dimethylation at Arg3. UVPD-PTCR exhibited large gains in characterization for other histones, such as histone H2A, increasing the sequence coverage from 59 to 77% for monoacetylated H2A.

■ INTRODUCTION

Analysis of intact proteins by top-down mass spectrometry (TDMS) affords the opportunity to capture variations within primary amino acid sequences, ^{1–4} chemical modifications, ^{5–8} and aberrant protein truncations that contribute to the diverse functions of various proteoforms. 9,10 Unique functional outcomes have been associated with the presence and absence of individual or multiple post-translational modifications (PTMs). 11,12 These structural additions modulate a protein's overall net charge, conformational state, and participation in cellular crosstalk. The impact of PTMs is especially marked in the canonical histone protein family—H2A, H2B, H3, and H4, overseers of intricate epigenetic mechanisms. The presence of multiple modifications (e.g., acetylation and methylation) across many histone subunits establishes a histone code that influences the recruitment of chromatinmodifying enzymes that remodel the chromatin structure ahead of transcriptional activation or repression. 15,16 Aberrant histone PTM patterns are hallmarks of many neurodegenerative diseases, 17 forms of cardiac hypertrophy, 18 and various cancers, 19 as misregulation of these PTMs disrupts proper cellular activity.20

Although high mass resolution and mass accuracy MS (e.g., Fourier transform mass spectrometry) allows accurate determination of an intact proteoform's molecular weight, sources of chemical and genetic variation can be inferred but not localized among the amino acid sequence, solely based on an intact mass measurement. Tandem mass spectrometry (MS/MS) is crucial for elucidating sequences and assigning

the locations of PTMs—the chief goal of histone proteomics. 21,22 The ability to fully characterize a histoform (i.e., histone proteoform) requires MS/MS strategies that provide extensive fragmentation of the protein backbone without the disruption of labile PTMs. In the context of top-down analysis of modified proteins, the most popular ion activation method, collision-induced dissociation (CID), yields sparse fragmentation, and labile PTMs are often detached during the activation process.²³ Alternative electron-based activation methods, such as electron capture dissociation (ECD) and electron-transfer dissociation (ETD), produce extensive fragmentation of intact proteins.^{24,25} The nonergodic nature of the radical-driven dissociation process enhances the probability of backbone cleavages throughout the protein while also successfully mapping multiple modifications that exist in combination with histone sequences.^{26–28} Implementation of supplemental activation, such as activated ion ETD, 29 and other hybrid activation methods, such as electron-transfer/higher-energy collisional dissociation (EThcD),³⁰ have further extended the performance metrics of electron-based activation methods.

Received: December 27, 2022 Accepted: March 17, 2023 Published: March 29, 2023





193 nm ultraviolet photodissociation (UVPD) has also demonstrated exceptional performance for the characterization of intact proteins and localization of PTMs.³¹ UVPD promotes many types of backbone cleavages, resulting in informative (and also dense) fragmentation patterns,³¹ and has been used successfully for the analysis of histones.^{32,33} The first UVPD study of intact histones compared the performance of 193 nm UVPD to higher-energy collisional dissociation (HCD, a beam-type CID method), finding that UVPD generated higher levels of sequence coverage for 80% of the analyzed bovine histoforms compared to HCD, with differences in sequence coverage between the two methods ranging from 5 to 65%.³² However, some histone proteoforms containing three to four modifications were undercharacterized by UVPD (i.e., Cscores <40 in which C-score³⁴ is a scoring metric developed to report the information content of MS/MS spectra in the context of characterization of proteoforms). This latter observation was also consistent with findings from other topdown studies of histones, including the largest core histone, H3, which tends to retain the most complicated modification state among the other histone family members.^{28,35} One prevalent factor noted upon UVPD of heavily modified histones is inadequate deconvolution of the most congested regions of the resulting MS/MS spectra, thus hampering fragment ion assignment.

The ability to resolve spectral complexity and increase the signal-to-noise (S/N) of fragment ions from large proteins (>30 kDa) has caused a resurgence in the use of gas-phase ionion reactions in recent years.^{36–43} The foundational framework for capitalizing on ion-ion chemistry to reduce the charge states of ions and disperse them over a broader region of the m/z landscape was established using proton transfer reactions (PTRs) in ion-trapping mass spectrometers over 25 years ago. 44,45 Since then, an array of other ion transformation strategies have been developed, including charge inversion and metal transfer reactions. 46,47 More recently, proton transfer charge reduction (PTCR) has been utilized to concentrate precursor ions of proteins into select charge states prior to activation or to enhance the ability to uncover fragment ions obscured in congested regions of MS/MS mass spectra. 36,37,39,42 PTCR has been employed for resolving co-eluting proteoforms during large-scale LC-MS/MS analysis, 38 integrated into multiple instrument platforms (e.g., FTICR instruments⁴¹ and Orbitrap platforms^{36–40,42,43,48,49}), and combined with UVPD for top-down protein analysis.^{40,48,49} In particular, following UVPD with PTCR alleviates the spectral congestion that most notably occurs in the region $\pm 100-250 \ m/z$ around the activated precursor ion, facilitating the identification of additional key sequence-determining fragment ions. 40 The UVPD-PTCR method afforded gains in sequence coverage in the central regions of proteins, which are typically difficult to characterize owing to the lack of assignable fragment ions.

Unveiling obscured fragment ions with PTCR presents an especially attractive method to better characterize modified proteins like histones, as demonstrated in one recent study.³⁷ In that landmark investigation, ETD was combined with ion/ion proton transfer (IIPT) reactions involving sulfur hexafluoride and multiple C-trap fills before Orbitrap mass analysis, resulting in substantially higher levels of signal-tonoise (S/N) of the fragment ions.³⁷ Using this approach, sequence coverage values as high as 81% were obtained for histone H4 containing five acetylations and one dimethylation

upon successful decluttering of crowded ETD mass spectra.³⁷ To advance the powerful combination of UVPD and PTCR for analyzing histones, the present study showcases the incorporation of UVPD-PTCR into an LC-MS workflow, boosting proteoform characterization metrics and decongesting complex MS/MS spectra for more confident characterization of histone proteoforms.

EXPERIMENTAL SECTION

Materials, Reagents, and Sample Preparation. Calf thymus histone extract (catalog no. 10223565001) and LC-MS-grade solvents were purchased from Sigma-Aldrich (St. Louis, MO). PTCR reagent, perfluoroperhydrophenanthrene (PFPP, *m/z* 624), was purchased from Oakwood Chemical (Estill, SC).

Liquid Chromatography-Mass Spectrometry. All experiments were performed on a Thermo Fisher Scientific Orbitrap Fusion Lumos Tribrid mass spectrometer modified to enable 193 nm UVPD using a 500 Hz ArF excimer laser (Coherent Excistar XS). The front-end reagent ion source, which allows the generation of ETD reagent ions, was also modified to introduce perfluoroperhydrophenanthrene (PFPP) for PTCR experiments, as described previously. 38,39 Reversedphase liquid chromatography was conducted using a Dionex UltiMate 3000 RSLCnano LC system (Thermo Fisher Scientific, San Jose, CA). Examples of chromatographic traces are presented in Figure S1. A single 1.5 mJ laser pulse was used for UVPD. Parameters used for collection of MS¹ and MS/MS spectra are provided in the Supporting Information. A subset of the proteoforms identified in the untargeted runs was added to an inclusion list for targeted activation and characterization using UVPD-PTCR (Table S1).

Data Analysis. The spectra acquired from untargeted LC-MS-UVPD runs were searched against the Bos taurus proteome comprising $\sim 3 \times 10^6$ total candidate proteoforms (UniProt Proteome ID: UP000009136) using Proteome Discoverer (PD) version 2.4.1.6. For the first data processing step, the ProSight PD (PSPD) Comprehensive Discovery Proteomics workflow was utilized. MS1 and MS2 spectra were deconvoluted using the high/high cRAWler algorithm (using a 10 ppm mass tolerance) and incorporated into annotated proteoform and subsequent searches. For the consensus processing step, the PSPD 1% FDR Consensus workflow was utilized. Highpriority PTMs as defined by PD were included in the database searches, including acetylation, phosphorylation, formylation, monomethylation, dimethylation, and trimethylation. The search nodes utilized during each processing step are displayed in Figure S2. Proteoforms activated during the targeted LC-MS runs using HCD, EThcD, UVPD, and UVPD-PTCR were also deconvoluted manually using the Xtract algorithm within Thermo Fisher Scientific FreeStyle version 1.5. TDValidator, which uses a protein's sequence to generate theoretical isotopic distributions, was employed to examine the experimental isotopic distributions and calculate the S/N of select fragment ions.⁵¹ Modifications found on the histones presented in this study are annotated according to the Brno nomenclature, which presents the protein and its modified residues as uppercase letters, while the modifications are lowercase.⁵² Additional details are provided in the Supporting Information.

RESULTS AND DISCUSSION

Despite the extensive body of work demonstrating the utility of PTCR reactions for the identification and characterization of intact proteins >30 kDa, there has been relatively little focus on its use for proteins containing PTMs. As protein size and/or modification state increases, the potential to produce more overlapping fragment ions increases greatly,⁵³ a factor that is particularly prominent for UVPD. The application and benefits of PTCR to charge-reduce fragment ions generated by UVPD of large proteins have been described previously, 40 and a similar strategy is utilized in the present study that focuses on histones and characterization of their PTMs. Briefly, following the activation of a selected charge state of an intact protein by UVPD, the resultant fragment ions are allowed to react with a proton-scavenging reagent anion for 10-15 ms, reducing their charge states and thus dispersing the fragment ions over a broader m/z range. We strategically segment the UVPD mass spectrum into two large m/z sections, applying PTCR to the most congested fragment ion regions and circumventing undesirable charge reduction of the abundant precursor ion. The two sections were termed "lower m/z isolation window" and "higher m/z isolation window" or "lower window" and "higher window" hereafter. This protocol was integrated into an LC-MS workflow according to the strategy illustrated in Figure 1. Following nano-LC-MS of calf thymus core histones

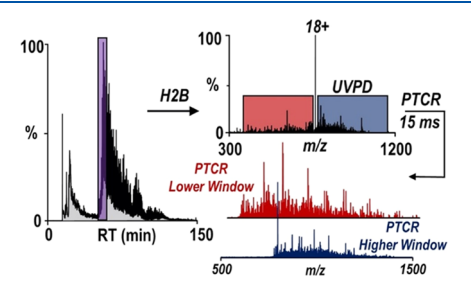


Figure 1. LC-MS-UVPD-PTCR process using two isolation windows. Calf thymus histone proteoforms separated by online reversed-phase nano-LC-MS were selected for UVPD activation using a single 1.5 mJ pulse. UVPD-generated fragment ions $\pm 110~m/z$ away from the activated precursor ion were isolated using a window size of 200~m/z and subjected to PTCR (reaction time of 15 ms). The shaded boxes (red and blue) represent separate isolation windows used to generate two unique UVPD-PTCR MS³ spectra.

(H2A: 13.9 kDa, H2B: 13.7 kDa, H3: 15.3 kDa, and H4: 11.3 kDa), charge states corresponding to each respective histone protein and their proteoforms were targeted for UVPD activation (single 1.5 mJ pulse). In succession, two subsequent isolation steps and PTCR periods were performed in the linear ion trap following UVPD. Each isolation window was centered on 110 m/z units on both sides of the activated precursor ion, utilizing a width of 200 m/z for each window. PTCR was performed on each section of the isolated fragment ions for 15 ms, resulting in charge-reduced product ions that were transferred to the Orbitrap for high-resolution mass analysis. This process was repeated on each histone proteoform target while sequentially moving throughout the chromatographic run, decluttering the most congested regions of the UVPD mass spectra.

A mixture of core histones was separated by LC-MS and analyzed by multiple activation methods, including HCD, EThcD, UVPD, and UVPD-PTCR. Histone H4, known to

harbor combinations of methylation and acetylation marks, was targeted between minutes 60 and 70 (Figure S3). Figure S4 illustrates the examples of mass spectra from each fragmentation method as well as companion sequence coverage maps generated from the fragment ions. Among the H4 proteoforms that were discovered, one H4 proteoform contained mass shifts consistent with the addition of acetyl and dimethyl groups. Reported in a prior study from 2018 using a top-down UVPD-MS approach,³² acH4R3me2K12ac was analyzed by HCD, EThcD, UVPD, and UVPD-PTCR (Figure 2). UVPD-PTCR generated near-complete sequence coverage (91%), with a large array of fragment ions throughout the entire sequence (Figure 2A). Many matching fragment ions gained from UVPD-PTCR originated from the higher UVPD-

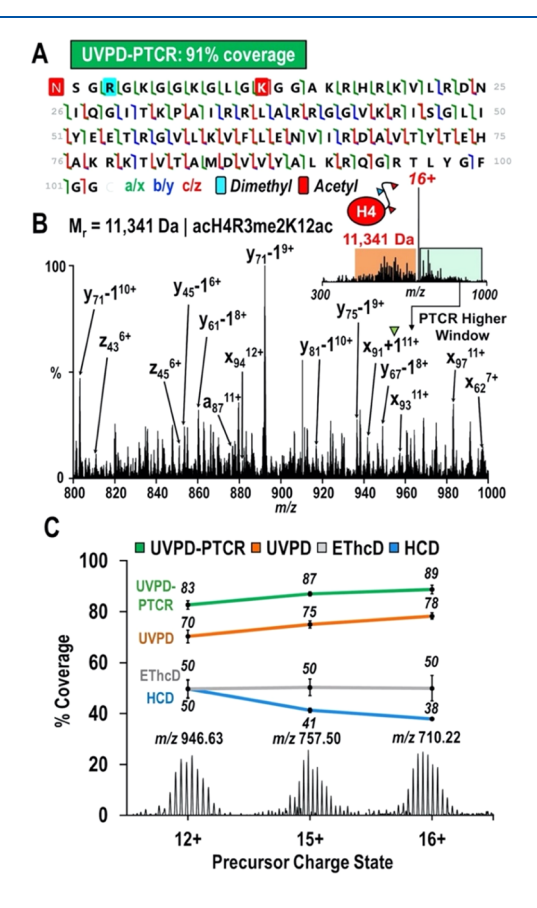


Figure 2. Characterization of modified histone H4 proteoform. (A) Sequence coverage map of acH4R3me2K12ac ($M_r = 11,341.46$ Da, m/z 710.2266, z = 16) following UVPD-PTCR (P-score: 4.8 \times 10⁻²¹⁷; proteoform characterization score (PCS): 2,749.43; 233 matching fragment ions). Sequence ions identified following PTCR of the higher window are annotated in panel (B), which shows an expansion of m/z 800–1000. One PTM-bracketing fragment ion, x_{91} + 111+, that supports the localization of K12ac is highlighted with a green triangle. The entire UVPD-PTCR spectrum from panel (B) (higher window) is shown in Figure S4C. (C) Average sequence coverage obtained from triplicate data sets of stepped HCD (20 \pm 5% NCE), EThcD (ETD: 7 ms; HCD: 12% NCE), UVPD (1 pulse, 1.5 mJ), and UVPD-PTCR (UVPD: 1 pulse, 1.5 mJ; PTCR: 15 ms) of three precursor charge states (m/z 946.6312, z = 12; m/z 757.5021, z= 15; m/z 710.2266, z = 16). Insets: expansion of acH4R3me2K12ac precursor ion in each respective charge state. The corresponding spectra and lists of fragment ions gained from HCD, EThcD, UVPD, and UVPD-PTCR are shown in Figure S4 and Tables S2-S6, respectively.

PTCR window (isolation and PTCR of the m/z 720–920 region), yielding numerous C-terminal ions from m/z 800 to 1000 (Figure 2B).

The sequence coverages following activation of three precursor ion charge states (12+, 15+, and 16+, average of three replicates for each) of acH4R3me2K12ac using HCD, EThcD, UVPD, and UVPD-PTCR are summarized in Figure 2C. On average, for the 16+ charge state, HCD yielded the lowest sequence coverage (38%), followed by EThcD (50%), UVPD (78%), and UVPD-PTCR (89%). Other proteoform scoring metrics, including the proteoform characterization scores (PCS) from all three charge states using the four tandem MS methods, are summarized in Figure S5 and Table S1. Fragment ions identified from HCD, EThcD, UVPD, and UVPD-PTCR are listed in Tables S2-S6. The theoretical and experimental isotopic profiles of key PTM-bracketing fragment ions, such as the C-terminal ion, x_{99} , were analyzed and confirmed by TDValidator (one example is shown in Figure S6).

Comparing the performance of UVPD and UVPD-PTCR from one replicate, UVPD generated 80% sequence coverage for the 16+ charge state based on 120 total matching fragments (Figure S4A). When PTCR was performed on the section of fragment ions lower in m/z than the precursor (i.e., lower window), 63% sequence coverage was obtained based on the detection of 85 matching fragment ions (Figure S4B). PTCR of the region higher in m/z than the precursor (i.e., higher window) led to the recovery of 107 matching fragments that afforded a 70% sequence coverage (Figure S4C). The best proteoform characterization was obtained by combining the standard UVPD spectrum and the two UVPD-PTCR spectra obtained from the lower and higher windows, yielding 91% sequence coverage and 233 fragment ion identifications. The sequence coverage and number of matching fragments from the lower and higher windows were compared before and after PTCR (Figure 3). Conducting PTCR on the higher window consistently led to larger gains in sequence coverage compared to the lower window (Figure 3A).

A comparison of the sequence coverages from the lower window before and after PTCR revealed that the sequence coverage showed little or no change for any of the charge states (12+, 15+, 16+). Much larger gains in sequence coverage, ranging from 11 to 28%, were obtained for all three charge states following PTCR of the higher window. The outcomes in sequence coverage can be attributed to the number of matching fragments uncovered in each window; the higher PTCR window demonstrated the greatest increase in the number of matching fragments, up to 27-68 additional fragment ions, compared to the lower PTCR window following UVPD (Figure 3B). When combining fragment ions acquired from UVPD and UVPD-PTCR spectra from different precursor charge states, the absolute sequence coverage did not change significantly. For instance, concatenating fragments from a UVPD spectrum with a precursor charge state of 16+ and PTCR lower/higher windows with precursors in the 12+ charge state, sequence coverage remained at 91%. Similarly, a sequence coverage of 91% was observed when incorporating fragment ions gained from UVPD-PTCR higher (12+) and UVPD-PTCR lower (15+) windows to the UVPD spectrum

As UVPD-PTCR uncovers many additional fragments, it is important to consider how the increased number of product ions affects the false discovery rate. This is particularly

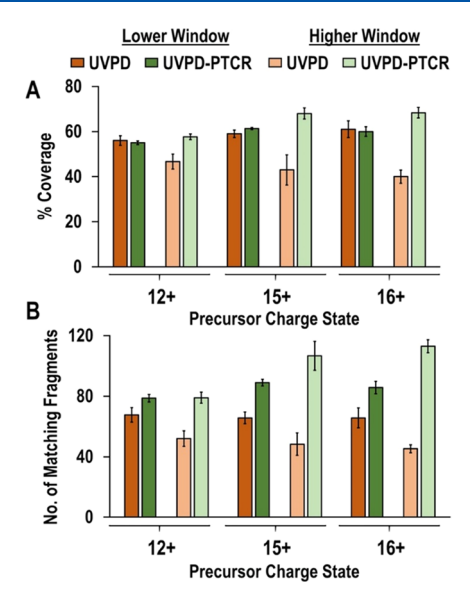


Figure 3. Sequence coverage and number of matching fragments obtained from the lower and higher UVPD and UVPD-PTCR windows: acH4R3me2K12ac. Average (A) sequence coverage and (B) number of matching fragments gained from UVPD and UVPD-PTCR of the 12+, 15+, and 16+ precursor charge states.

problematic for histones, as the myriad of PTM combinations to consider could lead the software to assign false hits. The S/ N threshold used to deconvolute spectra and fragment mass tolerance used for fragment ion identification are two parameters that can be altered to monitor the presence of false-positive identifications. 51 To examine the effect of the S/ N threshold, UVPD-PTCR spectra of acH4R3me2K12ac (16+) were deconvoluted at multiple S/N values and plotted against the $-\log(P\text{-score})$ and sequence coverage, as shown in Figure S7. As expected, the sequence coverage and $-\log(P$ scores) decline when using fragment mass tolerances below 5 ppm, whereas sequence coverage increases when using a fragment mass tolerance of 5–10 ppm (Figure S7A). Although the decline in sequence coverage for fragment mass tolerances <5 ppm and the boost in sequence coverage between 5 and 10 ppm may suggest an increase in false positives, the fact that the $-\log(P\text{-scores})$ remain high suggests otherwise (Figure S7B). Utilizing a fragment mass tolerance of ±10 ppm for sequence matching, the sequence coverage and $-\log(P\text{-scores})$ remained consistent across different S/N thresholds, suggesting that most fragment ions identified at S/N of 3 (the threshold used for this study) are legitimate identifications (Figure S7C,D). These metrics were also compared alongside HCD, EThcD, and UVPD, for which many of the trends were similar.

To decipher which ion types contributed most greatly to the additional matching fragments obtained from UVPD-PTCR of acH4R3me2K12ac, fragment ions that were found exclusively in the UVPD-PTCR data set were tallied and categorized according to their ion type (Figure 4A). A large portion of the additional matching fragments were C-terminal ions, with x-type ions comprising the majority, followed by y- and z-type ions. Among the fragment ions retaining the N-terminus, the number of a-type ions exceeded the portion of b- and c-type ions on average. Considering the consistent increase in sequence coverage and number of identified fragment ions from the higher PTCR window, a small region of the spectrum spanning m/z 763–771 was compared for UVPD and UVPD-

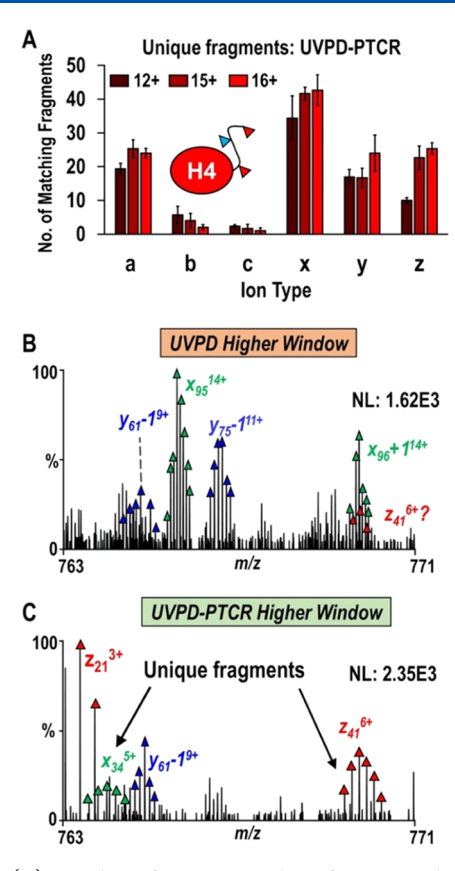


Figure 4. (A) Number of unique matching fragments obtained from UVPD-PTCR separated according to the ion type and precursor ion charge state. The a + 1, x + 1, and y - 1 ions were concatenated with the a, x, and y ions, respectively. Matching fragment ions identified within the (B) UVPD and (C) UVPD-PTCR higher windows between m/z 763 and 771. Annotation of this region by TDValidator is presented in Figure S8.

PTCR (Figure 4B,C). UVPD-PTCR revealed two additional C-terminal ions, $x_{34}^{\rm S+}$ and $z_{41}^{\rm 6+}$, in Figure 4C that were uncovered due to the removal of confounding background species and the abundant x_{96} + 1¹⁴⁺ ion upon UVPD (Figure 4B). The theoretical and experimental isotopic distributions of these fragment ions from acH4R3me2K12ac (16+) are presented in Figure S8 from TDValidator. Plotting the m/z values of the matching fragment ions gained from UVPD and UVPD-PTCR against their respective charge states, the decreased spectral congestion derives from the overall reduction in charge states of the UVPD-generated fragment ions and their increased dispersion across the m/z space (Figure S9).

The lower and higher UVPD-PTCR windows were further investigated to delineate the types of fragment ions present in each window. The distribution of ion types for the three charge states (12+, 15+, 16+) of acH4R3me2K12ac is shown in Figure 5. All nine ion types were found in both windows; however, the distribution of ion types varied significantly. Generally, N-terminal fragment ions (a/a + 1, b, c) dominated the lower UVPD-PTCR window, whereas C-terminal ions (x/x + 1, y/y - 1, z) were prevalent in the higher UVPD-PTCR window.

Furthermore, the higher UVPD-PTCR windows contained an abundance of *x*-type ions among the other C-terminal ions, and *a*-type ions dominated the lower UVPD-PTCR windows compared to the *b*- and *c*-type ions. This trend also held true

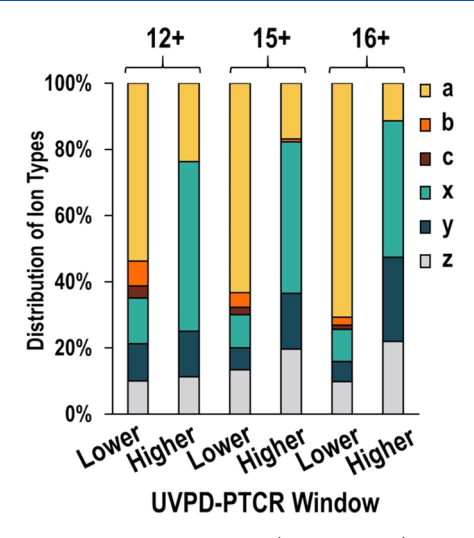


Figure 5. Distribution of N-terminal (a/a + 1, b, c) and C-terminal (x/x + 1, y/y - 1, z) fragment ion types identified within the lower and higher UVPD-PTCR windows from histone acH4R3me2K12ac $(M_r = 11,341.46 \text{ Da}, z = 12, 15, 16)$. The a + 1, x + 1, and y - 1 ions were concatenated with the a, x, and y ions, respectively. All percentages reflect the number of each ion type averaged from three UVPD-PTCR replicates for each window.

for another H4 proteoform containing an N-terminal acetylation and dimethylation mark at R3 (acH4R3me2) (Figure S10) as well as for the other histones that were analyzed in this study, H2A and H2B (Figures S11 and S12). This partitioning of the N-terminal and C-terminal ions into the lower and higher windows, respectively, was also observed for UVPD without PTCR (Figure S13) as well as for EThcD (Figure S14A) and HCD (Figure S14B) of histones in higher charge states. Thus, the preferential residence of N-terminal and C-terminal ions within the lower and higher windows is not a unique consequence of UVPD and could be a general pattern for histones. This outcome is likely related to the uncommonly large number of basic residues in the histone's Nterminal tail that leads to higher charge states and lower m/zvalues for the N-terminal fragment ions, shifting them to a region of lower m/z in relation to the precursor ion.

Due to the isobaric nature of histone proteoforms, the fragmentation patterns were matched to alternative H4 proteoforms to examine the outcomes (Figure S15). Histone H4 can be acetylated on the following residues: N-terminus, K5, K8, K12, K16, K31, K79, and K91. The following sequence coverages were gained from the following proteoforms: acH4R3me2K5ac: 85%; acH4R3me2K8ac: 88%, acH4R3me2-K12ac: 91%, acH4R3me2K16ac: 93%; acH4R3me2K31ac: 85%; acH4R3me2K79ac: 54%; acH4R3me2K91ac: 44%. Given the relatively high sequence coverages for each alternative proteoform, the presence of multiple proteoforms is plausible. In addition to the sequence coverage gained by UVPD-PTCR, the sequence coverage and number of matching fragment ions for each proteoform are presented in Figure S16. Focusing on acH4R3me2K16ac and comparing the results from UVPD and UVPD-PTCR, the difference in sequence coverage and number of matching fragment ions between the two methods were 12% and 114, respectively. Similar outcomes were observed for the other proteoforms that were investigated, such as acH4R3me2K8ac for which the sequence coverage and number of matching fragment ions were increased by 12% and 111, respectively, following UVPD-

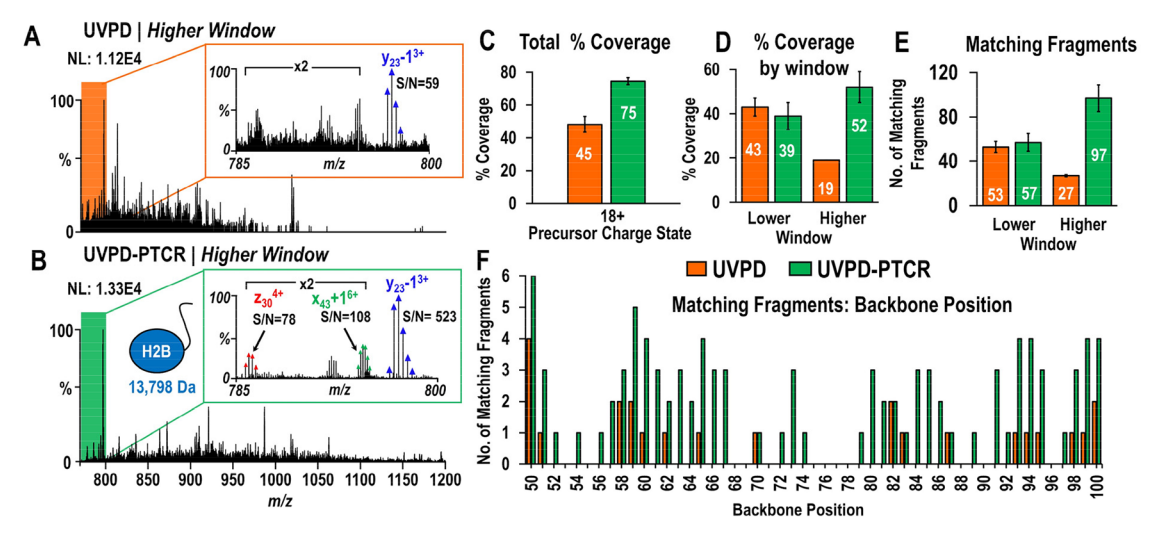


Figure 6. Characterization of unmodified H2B variant using UVPD and UVPD-PTCR. Expansion of region m/z 785–1200 following (A) UVPD of H2B ($M_{\rm r}=13,798.53$ Da, m/z 767.9786, z=18) and (B) UVPD-PTCR. Insets: assignment of fragment ions (outlined with shaded triangles) between regions m/z 785 and 800. Average sequence coverage following (C) three replicates of UVPD and UVPD-PTCR for the 18+ charge state. Average (D) sequence coverage and (E) matching fragments derived from either the lower/higher UVPD window or lower/higher UVPD-PTCR window. (F) Comparison of the number of matching fragments generated at each backbone position of H2B (from residues 50 to 100) following UVPD. Representative mass spectra and summaries of fragment ions are shown in Figure S28 and Tables S17–S21. The entire backbone cleavage map displaying residues 1-125 is presented in Figure S31.

PTCR. 91% sequence coverage/233 matching fragments and 93% sequence coverage/235 matching fragments were uncovered for acH4R3me2K12ac and acH4R3me2K16ac, respectively. UVPD-PTCR demonstrated support for both proteoforms, solidified by the presence of PTM-bracketing ions near the acetylation marks at K12 and K16. The sequence coverages were also segmented according to UVPD-PTCR lower and upper windows in Figure S17 for acH4R3me2-K12ac, acH4R3me2K16ac, and acH4R3me2K8ac. From these results, UVPD-PTCR demonstrates an ability to map additional histone codes with more confidence than UVPD, HCD, or EThcD.

Three charge states of another H4 proteoform, acH4R3me2 ($M_{\rm r}=11,299.47$ Da, m/z 943.1248, z=12; m/z 870.6542, z=13; m/z 754.7011, z=15), were targeted for UVPD-PTCR analysis. The results are summarized in Figures S18—S22 and Tables S7—S11. The application of the UVPD-PTCR strategy for other H4 histones with more complex PTM codes, such as those analyzed by traditional fragmentation methods, $^{27,28,32,54-56}$ is underway.

The UVPD-PTCR strategy was also applied to histones H2A and H2B, larger proteins whose midsections are sometimes difficult to characterize during top-down LC-MS/ MS. Often found to be minimally modified, H2A and H2B are usually categorized according to their level of variation from their canonical sequences. Bovine H2A, for instance, comprises several variants including macroH2A, H2A.z, and H2A types 1 and 2-C. We set out to characterize H2A type-1 among the other proteoforms that were discovered at levels of lower abundance (Figure S23). Examples of HCD, EThcD, UVPD, and UVPD-PTCR spectra are shown in Figure S24 for the 18+ charge state, and comparisons of sequence coverages, number of matching fragment ions, and PCS scores are summarized in Figure S25. Fragment ion lists from each method are summarized in Tables S12-S16. Similar levels of sequence coverage were obtained for both UVPD (59%) and EThcD (56%) (Figure S24A,D). Stepped HCD provided the lowest coverage (32%) due to the sparse number of fragment ions near the N-terminus and midsection of the sequence (Figure S24E). UVPD-PTCR uncovered many new fragment ions, yielding sequence coverages as high as 48 and 59% from the lower and higher UVPD-PTCR windows (Figure S24B,C). The benefit of conducting PTCR of both regions of the UVPD spectrum is evident in the sequence coverage map displayed in Figure S26, for which the sequence coverage increased from 59% (UVPD without PTCR) to 77% (UVPD-PTCR). Portions of the acH2A sequence in which the sequence coverage was enhanced are boxed in a gray overlay in Figure S26B. Significantly more fragment ions were identified in the latter half of the sequence, covering residues 76–126.

Given the increased characterization afforded by UVPD-PTCR of H2A (\sim 14 kDa), we anticipated similar gains for histone H3 (\sim 15 kDa). However, histone H3 suffered from inadequate signal, and thus extensive fragmentation was not achieved. For instance, we targeted a previously reported H3 proteoform: H3.1R2me2K4acR8me2 (15361.49 Da, m/z732.9857, z=21). The sequence coverages obtained from these experiments were 19% (HCD), 13% (EThcD), 10% (UVPD), and 18% (UVPD-PTCR), which proved insufficient to truly characterize these proteins. As it stands, optimizing the method to characterize larger, more heavily modified proteoforms such as H3 serves as a future goal.

Three H2B variants, H2B type-1, H2B type-1-N, and H2B, were detected in the calf thymus core histone extract (Figure S27). The 18+, 19+, and 20+ charge states of H2B ($M_{\rm r}$ = 13,798.53 Da) were selected for activation, and examples of the resulting spectra are shown in Figure S28. Sequence coverage was highest for all activation methods in the 18+ charge state (m/z 767.9786) (Figure S29). HCD of the 18+ precursor yielded 43 matching fragments, 29% sequence coverage, and a PCS of 462 on average. Uniquely for H2B, EThcD outperformed UVPD for all three precursor charge states, providing an additional 9% in average sequence coverage and 19 more matching fragment ions. Due to the large array of ion types generated by UVPD, low S/N and inadequate deconvolution of congested regions of the

spectrum hampered fragment ion assignment. For instance, Figure 6A,B displays the region from m/z 785 to 1200 following UVPD of the 18+ charge state of H2B before and after PTCR. Further expansion of the region from m/z 785 to 800 highlights the extreme density of fragment ions near the precursor ion observed in most UVPD spectra (inset of Figure 6A). PTCR (15 ms, higher UVPD-PTCR window) yields a less congested spectrum with fragment ions distributed to higher m/z (Figure 6B). Fragment ions z_{30}^{4+} and $x_{43} + 1^{6+}$ were uncovered after PTCR (inset of Figure 6B). The sequence maps generated by UVPD with and without PTCR are shown in Figure S30. Among the three replicates, the average sequence coverage was 75% for UVPD-PTCR compared to 45% for UVPD alone of the 18+ charge state (Figure 6C).

The sequence coverage and number of matching fragments (per UVPD and UVPD-PTCR window), as well as the resulting and backbone cleavage sites were compared for UVPD and UVPD-PTCR (Figure 6C-F). Most of the sequence coverage gained from UVPD was derived from fragment ions detected in the lower window (m/z range 182– 766), as UVPD generated 43% coverage (and 53 matching fragment ions) compared to 19% (27 matching fragment ions) for the higher window on average for H2B (18+) (Figure 6D,E). Performing PTCR on the lower window resulted in the uncovering of only four additional matching fragment ions and no gain in sequence coverage. PTCR of the higher window resulted in a >30% increase in sequence coverage (from 19 to 52%), and the number of matching fragment ions increased from 27 to 97 on average (Figure 6D,E). The gains in sequence coverage for UVPD-PTCR relative to UVPD alone are illustrated via the backbone cleavage diagram, which displays the number of fragment ions originating from cleavage of each backbone position for residues 50–100 (Figure 6F) and for the entire sequence (Figure S31). For instance, at backbone positions 72-74, UVPD generated no matching fragment ions, whereas UVPD-PTCR unveiled five matching fragment ions. The boost from PTCR generated higher amounts of sequence coverage and matching fragment ions compared to HCD, EThcD, or UVPD alone for all charge states of H2B (Figure S29) and resulted in considerably more coverage of the C-terminal half of the protein (Figure S30). In general, UVPD-PTCR provided access to a unique set of fragments that were not attainable through UVPD, EThcD, or HCD alone, including ions that fill in additional regions of the protein sequence.

■ CONCLUSIONS

UVPD provides exceptional sequence coverage and localization of modifications within histone sequences. 32 However, in cases in which HCD and EThcD outperformed UVPD, the S/N and spectral crowding of the resulting UVPD mass spectra were suspected as factors that limited the information gleaned from the UVPD mass spectra. Traditionally, the generation of more fragment ion types by UVPD (a/x, b/y, c/z) compared to that of HCD (b/y) or EThcD (b/y, c/z) results in higher sequence coverage of intact proteins but can lead to lower S/N and hamper deconvolution of extensively fragment-rich regions of UVPD-MS/MS spectra. Given the large improvements for the characterization of histones following charge reduction of ETD MS/MS spectra, including gains in both S/N and overall sequence coverage,³⁷ PTCR was coupled with UVPD to determine if similar outcomes could be obtained for histone proteoforms.

Compared to a previous study of intact histones based on 193 nm UVPD,³² applying UVPD-PTCR to smaller histones (e.g., H4: 11.3 kDa) yielded small gains in the overall sequence coverage. UVPD-PTCR produced drastic improvements in the overall P-scores and number of detected matching fragment ions, two factors that resulted in a more confident characterization of histone H4. Substantial enhancements in the proteoform scoring metrics for the larger histones (H2A: 13.9 kDa and H2B: 13.7 kDa) were also observed following the application of UVPD-PTCR. For the monoacetylated H2A proteoform (acH2A), for instance, an average sequence coverage of 73% was obtained from UVPD-PTCR compared to 61% for UVPD alone. Similar outcomes were demonstrated for H2B, as more sequence-determining fragment ions in both the midsection and terminal regions were detected following spectral clarification using PTCR. Moreover, UVPD promotes a greater array of backbone cleavages independent of the precursor charge state compared to HCD and ETD,³⁷ and thus the subsequent gains from PTCR are even more significant.

Our results demonstrate that coupling PTCR with UVPD offers several advantages for top-down proteomic analyses of histones. Reisolating fragment ions that reside in the most congested regions of a UVPD mass spectrum and subjecting them to PTCR allows the identification of additional fragments that enhance the characterization of histone sequences. The UVPD-PTCR method combines the high-performing proteoform characterization abilities of UVPD with the favorable spectral decluttering capabilities of PTCR, enriching the quality of sequence information that can be obtained from UVPD alone. Furthermore, UVPD-PTCR spectra uncovered additional product ions that allow for the identification of more isobaric species compared to HCD and EThcD.

Improvements in the throughput of the LC-MS-UVPD-PTCR method are likely to be achieved through the development of untargeted activation methods that will enable the characterization of more histone proteoforms per run. Although compromising the speed of analysis for depth of characterization, other LC-MS-UVPD-PTCR methods that incorporate multiple small windows of $50-60 \ m/z$ wide could be devised, allowing even more precise PTCR of overly fragment-rich regions.⁴⁰ Examining the utility of internal fragment ions for characterization of histone sequences is also an attractive pursuit as they may offer additional support for the presence and localization of certain modifications. However, due to the increased risk of detecting false-positive fragment ion identifications, the use of an internal calibrant during data acquisition (e.g., Easy-IC option on the Fusion Lumos) is essential to ensure high mass accuracy (<2 ppm) of the fragment ions. 57,58 Finally, applying UVPD-PTCR to histones with more combinatorial modifications is underway. Demonstrating the probability of reducing ambiguous hits and quantifying PTMs are goals of future studies. Overall, the ability of UVPD-PTCR to potentially characterize more challenging proteoforms (increasing mass and number of modifications) is another promising strategy to elucidate the sources of PTM variations that contribute to the enigma of the histone code.

ASSOCIATED CONTENT

Supporting Information

The Supporting Information is available free of charge at https://pubs.acs.org/doi/10.1021/acs.analchem.2c05765.

Total ion chromatograms from LC-MS experiments (Figure S1); summary of Proteome Discover data processing workflows (Figure S2); LC-MS analysis of calf thymus histones, H4 (Figure S3) H2A (Figure S23), and H2B (Figure S27); representative spectra from UVPD, UVPD-PTCR windows, EThcD, and HCD for H4 (Figures S4 and S19), H2A (Figure S24), H2B (Figure S28); sequence coverage maps from UVPD and UVPD-PTCR for acH4R3me2 (Figure S21), acH2A (Figure S26), and H2B (Figure S30); distribution of ion types generated by UVPD-PTCR of acH4R3me2 (Figure S10), acH2A (Figure S11), and H2B (Figure S12); distribution of ion types from UVPD of acH4R3me2K12ac (Figure S13); distribution of ion types generated by EThcD and HCD of acH4R3me2-K12ac (Figure S14); number of unique fragment ions gained from UVPD-PTCR of histone acH4R3me2, acH2A, and H2B (Figure S20); summary of HCD, EThcD, UVPD, and UVPD-PTCR proteoform scoring metrics for acH4R3me2K12ac (Figure S5), acH4R3me2 (Figure S18), acH2A (Figure S25), and H2B (Figure S29); change in sequence coverage and $-\log(P\text{-scores})$ as a function of fragment mass tolerance and S/N threshold for acH4R3me2K12ac (Figure S7); TDValidator analysis for acH4R3me2K12ac (Figures S6 and S8); plot of fragment ion charge states following PTCR (Figure S9); sequence coverage maps and number of matching fragments for isobaric H4 proteoforms acH4R3me2K12ac and acH4R3me2K16ac (Figure S15); sequence coverage maps and number of matching fragments for isobaric H4 proteoforms (Figure S16); sequence coverage maps for acH4R3me2K12ac, acH4R3me2K16ac, and acH4R3me2K8ac (Figure S17); average sequence coverage and number of Nterminal ions of histones H4, acH4, and acH4R3me2 following UVPD and UVPD-PTCR (Figure S22); number of matching fragments generated at each backbone position of H2B (from residues 1-125) following UVPD and UVPD-PTCR (Figure S31); targeted mass list and summary of sequence coverages obtained from HCD, EThcD, UVPD, and UVPD-PTCR and P-scores/PCS (UVPD-PTCR) for all histone proteoforms (Tables S1); lists of matching fragment ions from HCD, EThcD, UVPD, and UVPD-PTCR of acH4R3me2K12ac (Tables S2-S6); acH4R3me2 (Tables S7-S11); acH2A (Tables S12-S16); and H2B (Tables S17–S21) (PDF)

AUTHOR INFORMATION

Corresponding Author

Jennifer S. Brodbelt — Department of Chemistry, The University of Texas at Austin, Austin, Texas 78712, United States; orcid.org/0000-0003-3207-0217; Email: jbrodbelt@cm.utexas.edu

Authors

Jada N. Walker – Department of Chemistry, The University of Texas at Austin, Austin, Texas 78712, United States;

orcid.org/0000-0001-6233-3124

Raymond Lam – Department of Chemistry, The University of Texas at Austin, Austin, Texas 78712, United States;
orcid.org/0000-0003-1180-6846

Complete contact information is available at: https://pubs.acs.org/10.1021/acs.analchem.2c05765

Notes

The authors declare no competing financial interest.

ACKNOWLEDGMENTS

Funding from NSF (CHE-2203602), the Robert A. Welch Foundation (F-1155), and the UT System for support of the UT System Proteomics Core Facility Network is gratefully acknowledged. The authors thank Chad R. Weisbrod (National High Magnetic Field Laboratory), Christopher Mullen (Thermo Fisher Scientific), and John Syka (Thermo Fisher Scientific) for advice about implementation of PFPP as a PTCR reagent.

REFERENCES

- (1) Loo, J. A.; Edmonds, C. G.; Smith, R. D. Science 1990, 248, 201-204.
- (2) Shaw, J. B.; Li, W.; Holden, D. D.; Zhang, Y.; Griep-Raming, J.; Fellers, R. T.; Early, B. P.; Thomas, P. M.; Kelleher, N. L.; Brodbelt, J. S. J. Am. Chem. Soc. **2013**, 135, 12646–12651.
- (3) Toby, T. K.; Fornelli, L.; Kelleher, N. L. Annual Rev. Anal. Chem. **2016**, 9, 499-519.
- (4) Kaur, U.; Johnson, D. T.; Chea, E. E.; Deredge, D. J.; Espino, J. A.; Jones, L. M. Anal. Chem. 2019, 91, 142–155.
- (5) Siuti, N.; Kelleher, N. L. Nat. Methods 2007, 4, 817-821.
- (6) Lanucara, F.; Eyers, C. E. Mass Spectrom. Rev. 2013, 32, 27-42.
- (7) Aebersold, R.; Agar, J. N.; Amster, I. J.; Baker, M. S.; Bertozzi, C. R.; Boja, E. S.; Costello, C. E.; Cravatt, B. F.; Fenselau, C.; Garcia, B. A.; Ge, Y.; Gunawardena, J.; Hendrickson, R. C.; Hergenrother, P. J.; Huber, C. G.; Ivanov, A. R.; Jensen, O. N.; Jewett, M. C.; Kelleher, N. L.; Kiessling, L. L.; Krogan, N. J.; Larsen, M. R.; Loo, J. A.; Ogorzalek Loo, R. R.; Lundberg, E.; MacCoss, M. J.; Mallick, P.; Mootha, V. K.; Mrksich, M.; Muir, T. W.; Patrie, S. M.; Pesavento, J. J.; Pitteri, S. J.; Rodriguez, H.; Saghatelian, A.; Sandoval, W.; Schlüter, H.; Sechi, S.; Slavoff, S. A.; Smith, L. M.; Snyder, M. P.; Thomas, P. M.; Uhlén, M.; Van Eyk, J. E.; Vidal, M.; Walt, D. R.; White, F. M.; Williams, E. R.; Wohlschlager, T.; Wysocki, V. H.; Yates, N. A.; Young, N. L.; Zhang, B. Nat. Chem. Biol. 2018, 14, 206–214.
- (8) Compton, P. D.; Kelleher, N. L.; Gunawardena, J. J. Proteome Res. 2018, 17, 2727–2734.
- (9) Tvardovskiy, A.; Wrzesinski, K.; Sidoli, S.; Fey, S. J.; Rogowska-Wrzesinska, A.; Jensen, OleN. *Mol. Cell. Proteomics* **2015**, *14*, 3142–3153.
- (10) Chen, D.; Geis-Asteggiante, L.; Gomes, F. P.; Ostrand-Rosenberg, S.; Fenselau, C. J. Proteome Res. 2019, 18, 4013-4019.
- (11) Sharma, K.; D'Souza, R. C. J.; Tyanova, S.; Schaab, C.; Wiśniewski, J. R.; Cox, J.; Mann, M. Cell Rep. 2014, 8, 1583–1594.
- (12) Gregorich, Z. R.; Peng, Y.; Cai, W.; Jin, Y.; Wei, L.; Chen, A. J.; McKiernan, S. H.; Aiken, J. M.; Moss, R. L.; Diffee, G. M.; Ge, Y. J. Proteome Res. **2016**, 15, 2706–2716.
- (13) Venne, A. S.; Kollipara, L.; Zahedi, R. P. Proteomics 2014, 14, 513-524.
- (14) Leutert, M.; Entwisle, S. W.; Villén, J. Mol. Cell. Proteomics 2021, 20, No. 100129.
- (15) Strahl, B. D.; Allis, C. D. Nature 2000, 403, 41-45.
- (16) Jenuwein, T.; Allis, C. D. Science 2001, 293, 1074-1080.
- (17) Kwon, M. J.; Kim, S.; Han, M. H.; Lee, S. B. Mol. Cells 2016, 39, 783-789.
- (18) Liu, C.-F.; Tang, W. H. W. JACC Basic Transl. Sci. 2019, 4, 976–993.
- (19) Chervona, Y.; Costa, M. Am. J. Cancer Res. 2012, 2, 589–597. (20) Farrelly, L. A.; Thompson, R. E.; Zhao, S.; Lepack, A. E.; Lyu, Y.; Bhanu, N. V.; Zhang, B.; Loh, Y.-H. E.; Ramakrishnan, A.; Vadodaria, K. C.; Heard, K. J.; Erikson, G.; Nakadai, T.; Bastle, R. M.; Lukasak, B. J.; Zebroski, H.; Alenina, N.; Bader, M.; Berton, O.;

- Roeder, R. G.; Molina, H.; Gage, F. H.; Shen, L.; Garcia, B. A.; Li, H.; Muir, T. W.; Maze, I. *Nature* **2019**, *567*, 535–539.
- (21) Karch, K. R.; Sidoli, S.; Garcia, B. A.Identification and Quantification of Histone PTMs Using High-Resolution Mass Spectrometry. In *Methods in Enzymology*; Elsevier, 2016; Vol. 574, pp 3–29.
- (22) Karch, K. R.; Sidoli, S.; Garcia, B. A. Chapter One Identification and Quantification of Histone PTMs Using High-Resolution Mass Spectrometry. In *Methods in Enzymology*; Marmorstein, R., Ed.; Academic Press,, 2016; Vol. 574, pp 3–29.
- (23) Brodbelt, J. S. Curr. Opin. Chem. Biol. 2022, 70, No. 102180.
- (24) Riley, N. M.; Coon, J. J. Anal. Chem. 2018, 90, 40-64.
- (25) Zhurov, K. O.; Fornelli, L.; Wodrich, M. D.; Laskay, Ü. A.; Tsybin, Y. O. Chem. Soc. Rev. 2013, 42, 5014–5030.
- (26) Young, N. L.; DiMaggio, P. A.; Plazas-Mayorca, M. D.; Baliban, R. C.; Floudas, C. A.; Garcia, B. A. Mol. Cell. Proteomics 2009, 8, 2266–2284.
- (27) Pesavento, J. J.; Bullock, C. R.; LeDuc, R. D.; Mizzen, C. A.; Kelleher, N. L. J. Biol. Chem. 2008, 283, 14927–14937.
- (28) Zheng, Y.; Fornelli, L.; Compton, P. D.; Sharma, S.; Canterbury, J.; Mullen, C.; Zabrouskov, V.; Fellers, R. T.; Thomas, P. M.; Licht, J. D.; Senko, M. W.; Kelleher, N. L. *Mol. Cell. Proteomics* **2016**, *15*, 776–790.
- (29) Riley, N. M.; Westphall, M. S.; Coon, J. J. J. Proteome Res. 2017, 16, 2653–2659.
- (30) Brunner, A. M.; Lössl, P.; Liu, F.; Huguet, R.; Mullen, C.; Yamashita, M.; Zabrouskov, V.; Makarov, A.; Altelaar, A. F. M.; Heck, A. J. R. *Anal. Chem.* **2015**, *87*, 4152–4158.
- (31) Brodbelt, J. S.; Morrison, L. J.; Santos, I. Chem. Rev. 2020, 120, 3328–3380.
- (32) Greer, S. M.; Brodbelt, J. S. J. Proteome Res. 2018, 17, 1138–1145.
- (33) Greer, S. M.; Sidoli, S.; Coradin, M.; Schack Jespersen, M.; Schwämmle, V.; Jensen, O. N.; Garcia, B. A.; Brodbelt, J. S. *Anal. Chem.* **2018**, *90*, 10425–10433.
- (34) LeDuc, R. D.; Fellers, R. T.; Early, B. P.; Greer, J. B.; Thomas, P. M.; Kelleher, N. L. *J Proteome Res* **2014**, *13*, 3231–3240.
- (35) Thomas, C. E.; Kelleher, N. L.; Mizzen, C. A. J. Proteome Res. **2006**, *5*, 240–247.
- (36) Anderson, L. C.; English, A. M.; Wang, W.-H.; Bai, D. L.; Shabanowitz, J.; Hunt, D. F. *Int. J. Mass Spectrom.* **2015**, 377, 617–624.
- (37) Anderson, L. C.; Karch, K. R.; Ugrin, S. A.; Coradin, M.; English, A. M.; Sidoli, S.; Shabanowitz, J.; Garcia, B. A.; Hunt, D. F. Mol. Cell. Proteomics 2016, 15, 975–988.
- (38) Huguet, R.; Mullen, C.; Srzentić, K.; Greer, J. B.; Fellers, R. T.; Zabrouskov, V.; Syka, J. E. P.; Kelleher, N. L.; Fornelli, L. *Anal. Chem.* **2019**, *91*, 15732–15739.
- (39) Ugrin, S. A.; English, A. M.; Syka, J. E. P.; Bai, D. L.; Anderson, L. C.; Shabanowitz, J.; Hunt, D. F. J. Am. Soc. Mass Spectrom. 2019, 30, 2163–2173.
- (40) Sanders, J. D.; Mullen, C.; Watts, E.; Holden, D. D.; Syka, J. E. P.; Schwartz, J. C.; Brodbelt, J. S. Anal. Chem. 2020, 92, 1041–1049.
- (41) Weisbrod, C. R.; Anderson, L. C.; Hendrickson, C. L.; Schaffer, L. V.; Shortreed, M. R.; Smith, L. M.; Shabanowitz, J.; Hunt, D. F. Anal. Chem. 2021, 93, 9119–9128.
- (42) Kline, J. T.; Mullen, C.; Durbin, K. R.; Oates, R. N.; Huguet, R.; Syka, J. E. P.; Fornelli, L. *J. Am. Soc. Mass Spectrom.* **2021**, *32*, 2334–2345.
- (43) Bailey, A. O.; Huguet, R.; Mullen, C.; Syka, J. E. P.; Russell, W. K. Anal. Chem. **2022**, 94, 3930–3938.
- (44) Stephenson, J. L.; McLuckey, S. A. J. Am. Chem. Soc. 1996, 118, 7390-7397.
- (45) Stephenson, J. L.; McLuckey, S. A. Anal. Chem. 1998, 70, 3533-3544.
- (46) He, M.; Emory, J. F.; McLuckey, S. A. Anal. Chem. 2005, 77, 3173–3182.
- (47) Foreman, D. J.; McLuckey, S. A. Anal. Chem. 2020, 92, 252-266.

- (48) Holden, D. D.; Brodbelt, J. S. Anal. Chem. **2016**, 88, 12354–12362.
- (49) Holden, D. D.; McGee, W. M.; Brodbelt, J. S. Anal. Chem. 2016, 88, 1008-1016.
- (50) Klein, D. R.; Holden, D. D.; Brodbelt, J. S. Anal. Chem. 2016, 88, 1044–1051.
- (51) Fornelli, L.; Srzentić, K.; Huguet, R.; Mullen, C.; Sharma, S.; Zabrouskov, V.; Fellers, R. T.; Durbin, K. R.; Compton, P. D.; Kelleher, N. L. *Anal. Chem.* **2018**, *90*, 8421–8429.
- (52) Talbert, P. B.; Ahmad, K.; Almouzni, G.; Ausió, J.; Berger, F.; Bhalla, P. L.; Bonner, W. M.; Cande, W. Z.; Chadwick, B. P.; Chan, S. W. L.; Cross, G. A. M.; Cui, L.; Dimitrov, S. I.; Doenecke, D.; Eirin-López, J. M.; Gorovsky, M. A.; Hake, S. B.; Hamkalo, B. A.; Holec, S.; Jacobsen, S. E.; Kamieniarz, K.; Khochbin, S.; Ladurner, A. G.; Landsman, D.; Latham, J. A.; Loppin, B.; Malik, H. S.; Marzluff, W. F.; Pehrson, J. R.; Postberg, J.; Schneider, R.; Singh, M. B.; Smith, M. M.; Thompson, E.; Torres-Padilla, M.-E.; Tremethick, D. J.; Turner, B. M.; Waterborg, J. H.; Wollmann, H.; Yelagandula, R.; Zhu, B.; Henikoff, S. *Epigenet. Chromatin* **2012**, *5*, No. 7.
- (53) Compton, P. D.; Zamdborg, L.; Thomas, P. M.; Kelleher, N. L. Anal. Chem. **2011**, 83, 6868–6874.
- (54) Contrepois, K.; Ezan, E.; Mann, C.; Fenaille, F. J. Proteome Res. **2010**, *9*, 5501–5509.
- (55) Gargano, A. F. G.; Shaw, J. B.; Zhou, M.; Wilkins, C. S.; Fillmore, T. L.; Moore, R. J.; Somsen, G. W.; Paša-Tolić, L. *J. Proteome Res.* **2018**, *17*, 3791–3800.
- (56) Tian, Z.; Tolić, N.; Zhao, R.; Moore, R. J.; Hengel, S. M.; Robinson, E. W.; Stenoien, D. L.; Wu, S.; Smith, R. D.; Paša-Tolić, L. *Genome Biol.* **2012**, *13*, R86.
- (57) Dunham, S. D.; Wei, B.; Lantz, C.; Loo, J. A.; Brodbelt, J. S. *J. Proteome Res.* **2023**, 22, 170–181.
- (58) Schmitt, N. D.; Berger, J. M.; Conway, J. B.; Agar, J. N. Anal. Chem. **2021**, 93, 6355–6362.

☐ Recommended by ACS

Top-Down Ion Mobility Separations of Isomeric Proteoforms

Francis Berthias, Ole N. Jensen, et al.

DECEMBER 23, 2022

ANALYTICAL CHEMISTRY

READ 🗹

Online 2D High-pH and Low-pH Reversed-Phase Nano-LC-MS/MS System for Deep Proteome Analysis

Yu-Ching Liu and Chao-Jung Chen

MARCH 30, 2023

ANALYTICAL CHEMISTRY

RFAD 🗹

Enhanced Spatial Mapping of Histone Proteoforms in Human Kidney Through MALDI-MSI by High-Field UHMR-Orbitrap Detection

Kevin J. Zemaitis, Ljiljana Paša-Tolić, et al.

SEPTEMBER 06, 2022

ANALYTICAL CHEMISTRY

READ 🗹

CPPA: A Web Tool for Exploring Proteomic and Phosphoproteomic Data in Cancer

Guo-sheng Hu, Wen Liu, et al.

DECEMBER 12, 2022

JOURNAL OF PROTEOME RESEARCH

READ 🗹

Get More Suggestions >